

INTERACTIVE EFFECTS OF REACTIVITY AND MELT FLOW IN LASER MACHINING

Kai Chen, Y. Lawrence Yao
Department of Mechanical Engineering
Columbia University
New York, NY 10027

Abstract

A numerical model is developed to study the oxidation effects in oxygen-assisted laser cutting of mild steel. Coupled oxygen concentration and energy balance equations are solved by a control-volume based computational scheme while the velocity field is obtained by analytical boundary theory. Theoretical explanation on striation formation is given based on an instability analysis of the molten front. The striation frequency and depth are predicted. The steady-state simulation results include the temperature and oxygen concentration profiles at the cut front, the effects of impurity gas on the cutting speed, reaction energy, conduction loss, and heat affected zone. The dynamic simulation shows the oscillation of the molten temperature that is related to striations. The striation frequency and depth are experimentally validated.

1. Introduction

Modeling of the laser cutting process has been addressed by many investigators to help understand the phenomena and basic mechanisms involved and predict the effects of process parameters (Modest and Abakians, 1986; Schulz, *et al.*, 1993; Cai and Sheng, 1996). Most of the above models, however, pertain only to inert gas cutting, whereas in majority of industrial practice, laser cutting of metals uses oxygen as an assist gas to provide exothermic energy and to help increase cutting speed. It is commonly accepted that the reaction energy contributes nearly

half of the total energy input in reactive cutting of thin materials (Vicanek and Simon, 1987). The oxygen energy plays a more dominant role in thick section cutting (Fukaya and Norio, 1990). It is observed that a small amount of contamination in the oxygen jet will greatly reduce the cutting speed (Powell, *et al.*, 1992). However, most of these studies were based on experimental investigations. In models that dealt with oxygen assisted cutting, it is common that a fixed percentage of material participating in the reaction was assumed (Shuocker, 1986, Di Pietro and Yao, 1995). Molian and Baldwin (1992) used a mixture of acetylene and oxygen to create combustion reactions in CO₂ laser cutting and found enhancement in cutting speed and quality mainly due to reduced viscosity of slag formed during cutting. Experimental results were correlated with simple theoretical models. Espinal and Kar (1998) presented a more comprehensive energy balance model for chemical reaction in laser cutting. However, their approach assumes all the ejected melt partaking in reaction and thus the reaction energy is simply a multiplication of ejected mass and heat of reaction, which is not accurate in describing the reaction. Yilbas and Sahin (1995) reported a theoretical solution of the chemical reaction effects on heat transfer in the laser cutting process. The analysis, however, does not consider the diffusion processes inside the gas phase and liquid phase. Based on a previous study (Chen, Yao, and Modi, 1999), this paper presents a numerical model which will lead to more quantitative and in-depth understanding as well as prediction capabilities in oxygen-assisted laser cutting.

An important phenomenon in oxygen-assisted cutting is the formation of striation (Fig. 1), which has received much attention since the early stage of research on laser cutting because it strongly affects the cut quality. The explanations given for this phenomenon have been hydrodynamic instability (Vicanek, *et al.*, 1986), internal instability of the cutting process (Shuocker, 1986), cyclic oxidation (Arata, *et al.*, 1979, Ivarson, *et al.*, 1994). It is explained

(Arata, *et al.*, 1979, Ivarson, *et al.*, 1994) that, for diffusion controlled reaction, the rate of chemical reaction is time dependent, being rapid in the early stages but decreasing markedly as the thickness of the oxide layer increases. So the oxide layer will expand rapidly at first but slow down thereafter. Once the oxide is blown out from the cutting front, due to a sudden decrease of the oxide layer, another expansion will begin. Although this model gives a quite convincing explanation on the expansion of the oxide layer, it does not clearly explain how the oxide layer is suddenly reduced. A detailed investigation on the mechanism of the melt removal has led to more understanding or prediction of striation (Chen and Yao, 1999).

This current paper addresses the interactive nature of oxidation and melt flow in laser cutting. It first presents an oxidation model based on heat transfer, transport and chemical rate theory. By solving the coupled energy and oxygen concentration equations, the model is capable of describing the details of the oxidation process and estimating the effects such as reaction energy, and oxygen purity on cutting speed. A hydrodynamic instability analysis is then presented to investigate the dynamic process of the melt removal and it is shown that the molten front is hydrodynamicallly unstable. In conjunction with the wave frequency predicted by instability theory, temperature fluctuation caused by periodical removal of the molten layer is simulated and related to striation characteristics.

2. Theoretical Background of Simulation

2.1 Oxidation model

A simplified model is shown in Fig. 2. The workpiece is assumed to move at a constant speed in a direction perpendicular to the laser beam. Laser irradiation together with the reaction

energy heats up the metal and the gas jet exerts momentum on the molten material, leading to the ejection of the melt. It is assumed that

1. The solid and liquid are isotropic with homogeneous properties.
2. The main mechanism of material removal is melting and the effect of vaporization is neglected in this calculation.
3. The effect of plasma is not considered because of the relatively lower front temperature and a strong gas jet which continuously dissipates the plasma.
4. The radiative heat loss is neglected. It has been calculated by other existing models that the surface losses are negligible (Modest and Abakians, 1986).
5. The chemical reaction is of heterogeneous type and takes place at a single planar interface.

The mass transfer in the oxidation process mainly consists of i) the mass transfer from the bulk gas phase to the melt surface (i.e. from $x = \delta$ to $x = 0$ in Fig. 2); ii) the mass transfer in the reacted layer (from $x = 0$ to $x = i$); and iii) the first order reaction at the reaction plane ($x = i$).

The molten layer including the oxide layer is highly unstable under the high-speed gas jet. The simulation consists of two stages: 1. Steady state computation that assumes that the reaction occurs at the gas-liquid interface without the formation of an oxide layer, and 2. Time dependent calculation that assumes the growth of the oxide layer follows the well-known parabolic law for diffusion controlled reaction and the oxide layer is subsequently removed by hydrodynamic forces. The frequency of the removal cycle is calculated based on an instability theory presented in Section 3 below.

2.2 Governing equations and boundary conditions

a. Mass Balance

The governing equation for mass transfer in the gas phase is (neglecting diffusion in the x direction and convection in the y direction shown in Fig. 2):

$$c \frac{\partial X_{o_2}}{\partial t} + cu \frac{\partial X_{o_2}}{\partial x} = - \frac{\partial}{\partial y} N_{o_2}. \quad (1)$$

The oxygen diffusion consists of the molecular diffusion and the net bulk convection:

$$N_{o_2} = -cD_{o_2,g} \frac{\partial X_{o_2}}{\partial y} + X_{o_2} N_{o_2}. \quad (2)$$

A steady-state calculation is first carried out without taking into consideration of the oxide layer. In our transient calculation, a thin oxide layer with a large resistance is assumed to be present. The reaction is thus diffusion controlled and is largely dependent on the behavior of the oxide layer. The governing equation for mass transfer in liquid-phase oxide layer is:

$$c \frac{\partial X_{o_2}}{\partial t} + cu \frac{\partial X_{o_2}}{\partial x} = \frac{\partial}{\partial y} (cD_{o_2,m} \frac{\partial X_{o_2}}{\partial y}). \quad (3)$$

The boundary condition for the above described mass transfer is $X_{o_2} = X_{o_2,bulk}$ at the bulk gas stream ($x = \delta$, where δ is taken as $H/2$). At the reaction front i in Fig. 2, a first order chemical reaction leads to

$$N_{o_2} = k_r c (X_{o_2,i} - X_{o_2,e}). \quad (4)$$

The equilibrium concentration $X_{o_2,e}$ is obtained from the equilibrium constant K_e that is determined by Gibbs free energy of the reaction:



$$\Delta G_{rx}^o = -RT \ln K_e. \quad (6)$$

b. Energy Balance

The governing equation for heat transfer in the gas phase is in the parabolic form:

$$\rho_g \frac{\partial_p T}{\partial t} + \rho_g u \frac{\partial_p T}{\partial x} = \frac{\partial}{\partial x} \left(K_g \frac{\partial T}{\partial x} \right) + q_r + q_l. \quad (7)$$

The equation for heat transfer involving phase change in the material (both molten layer and solid) can be expressed in the enthalpy formulation:

$$\frac{\partial p h}{\partial t} + \frac{\partial p \Delta H}{\partial t} + \frac{\partial p u h}{\partial x} + \frac{\partial p u \Delta H}{\partial x} = \frac{\partial}{\partial y} \left(K \frac{\partial T}{\partial y} \right) + q_r + q_l, \quad (8)$$

where h is the sensible enthalpy defined as $h = h_{ref} + \int_{T_{ref}}^T c_p dT$ and ΔH is the latent heat content. It either varies with ΔH_m (latent heat) or is zero, depending upon whether the temperature exceeds the melting temperature. The laser heat source can be described by a Gaussian distribution function given by

$$q_l = P_l \exp\left[-\left(\frac{r}{r_l}\right)^2\right], \quad (9)$$

where P_l is the laser power density, r and r_l are distance from laser beam center and beam radius respectively. The average laser power density can be calculated accordingly. The reaction heat source is obtained from:

$$q_r = 2\Delta H_R N_{o_2}, \quad (10)$$

The boundary conditions for energy balance are that both the bulk gas temperature and the solid temperature far away from heat sources are equal to ambient temperature.

c. Momentum Balance

Instead of solving complex two-phase Navier-Stokes equations, the velocity field is obtained analytically from boundary layer theory. For the gas phase, the air velocity profile close to the liquid surface is assumed the same as that for turbulent flow in a smooth-walled channel, that is, follows the seventh-power velocity-distribution law (Schlichting, 1979):

$$\frac{u}{v^*} = 8.74 \left(\frac{-yv^*}{v_g} \right)^{\frac{1}{7}}, \quad (11)$$

where v^* is the friction velocity determined by

$$\frac{U_0}{v^*} = 8.74 \left(\frac{Hv^*}{2v_g} \right)^{\frac{1}{7}}. \quad (12)$$

The velocity profile in the melt phase is assumed linear and the surface velocity V_s is determined by matching the shear stress across the interface,

$$\rho_g v^{*2} = \frac{\mu V_s}{h}. \quad (13)$$

Since the exact behavior of the oxide layer under the effect of melt ejection is not well understood, a reasonable assumption is that the growth of the oxide layer for the diffusion controlled process follows the well known parabolic law:

$$\frac{ds}{dt} = BD \frac{\partial c}{\partial y}. \quad (14)$$

By assuming that the concentration on oxide surface is independent of the oxide film, Eq. (14) can be simplified to take the following quasi steady-state form:

$$\frac{ds}{dt} = BD \frac{c_0 - c_i}{s(t)} \approx BD \frac{c_0}{s(t)}, \quad (15)$$

The equation is then integrated to obtain the growth of the oxide layer. The combined coefficient of the above equation is not readily available and therefore it is calibrated so that the temperature fluctuation is around a level obtained from experiments (Arata, *et al.*, 1979).

Most physical properties concerned are temperature dependent and need to be updated during the calculation. The diffusivity of oxygen in the gas phase $D_{o2,g}$ is not affected by concentration for low to moderate pressure (<10 atm). It is dependent on the absolute temperature (T), the

pressure (P), the molecular weight (M) and the diffusion volume (V) of the impurity gas, and can be correlated as (Themelis, 1995):

$$D_{o_2,g} = \frac{0.001T^{1.75} \left(\frac{1}{M_{o_2}} + \frac{1}{M_{n_2}} \right)^{1/2}}{P(V_{o_2}^{1/3} + V_{n_2}^{1/3})^2} \quad (16)$$

The diffusivity of oxygen in the liquid (melt) phase takes the form of

$$D_{o_2,m} = D_{0,m} \exp(-E_a / RT). \quad (17)$$

The diffusivity of oxygen in liquid FeO is about $4 \times 10^{-4} \text{ cm}^2/\text{s}^{-1}$ at $1550 \text{ }^\circ\text{C}$ (Birks and Meier, 1983). It may however decrease as the ferric iron concentration increases. The coefficient $D_{0,m}$ in Eq. (17) is determined so that the diffusivity matches the above value. Data is not readily available for the oxidation rate of pure iron. An approximation is inferred from the experimental results of Robertson and Jenkins (1970). The reaction controlled experiment was conducted by levitating a 1 g sphere iron in an ample supply of oxygen. The rate corresponds to an oxidation flux of iron of $0.36 \text{ g}_{Fe} \text{ cm}^{-2} \text{ s}^{-1}$ at temperature of 1600°C . The oxygen flux (N_{o_2}) is thus about $0.10 \text{ g}_{o_2} \text{ cm}^{-2} \text{ s}^{-1}$ or $3.2 \times 10^{-3} \text{ mol cm}^{-2} \text{ s}^{-1}$. The equilibrium concentration can be neglected in this case and the kinetic rate constant is simply N_{o_2}/c , about $0.49 \times 10^3 \text{ cm s}^{-1}$.

The overall calculation domain and the boundary conditions are depicted in Fig. 3. A control-volume based discretization method is utilized to solve the coupled convection-diffusion problem. The detailed description of discretization of the parabolic governing equation is given by Patankar (1980). The two-dimensional discretization equations are written in the fully implicit forms. The power-law scheme is used here, which provides a good representation of the convection-diffusion behavior. The temperature or concentration dependent coefficients are linearized between each time step to facilitate the convergence.

3. Molten Front Instability & Striation Formation

3.1 Theoretical background

The behavior of a thin liquid film under gas flow has been studied over decades. Ripples are generated on the liquid surface when a high-velocity gas stream flows above a thick liquid layer, because the viscous dissipation is less than the energy transferred by the wave-induced pressure perturbation. The wave behavior depends on the gas velocity and the liquid flow rate. As the film thickness is reduced, the surface smoothes out because the friction in the liquid phase can overcome the pressure perturbation. When the film thickness is very small, it is found that the liquid film becomes unstable because the wave-induced shear stress perturbation is sufficient to overcome the restoring forces, and waves are generated on the liquid surface (Craik, 1966).

For the case of laser cutting of mild steel, it is commonly accepted that the molten front thickness is of the order of 10^{-5} m (Vicanek, 1986; Arata, 1979). For such an order of thickness, the molten front is unstable. Consider the top part of the molten front (Fig. 4). At low cutting speeds, the liquid film is exposed in the gas flow for a relatively long time in the gas flow and the liquid film will usually rupture since there is not enough liquid flow rate on the top part of the molten front. This phenomenon has been observed and described by Arata *et al.* (1979). When the cutting speed increases, the period of film rupture becomes shorter. At some critical cutting speed, there is not enough time for such instabilities to develop and therefore cause film rupture. Instead there is always a liquid film on the top of the molten front. This was described by Arata *et al.* (1979) as “steady cutting”, which corresponds to a cutting speed above 2m/min. This thin liquid film for mild steel of certain thickness, however, may still be unstable and instead of film rupture, slow waves may be generated (it is shown later that the thickness of the liquid film is

below the critical thickness under which slow waves are generated). Once the crest of the slow wave moves downwards from the top of the molten front, much more melt is removed and oxidation coupled with heat conduction begins to expand. The process is fast at first and slows down until another wave crest comes and moves the melt downwards. Thus an expansion-compression cyclic pattern is still formed above the so-called critical cutting speed. Melting and melt ejection are essentially coupled with each other to form a cyclic pattern at the molten front. It is obvious that the oscillation frequency of the molten front is related with the wave frequency on the molten front.

Instability occurs when the surface stress is sufficiently large to overcome the restoring forces of surface tension, that is (Craik, 1966):

$$\Pi_r + \frac{3\Sigma_i}{2kh} \geq \gamma k^2 h. \quad (18)$$

The critical thickness for stability can be evaluated for a given wavelength, if the perturbation shear stress can be calculated accordingly. Most theoretical analyses of interfacial instabilities have adopted Benjamin's quasi-laminar estimate (Benjamin, 1966). Benjamin's method is expected to give correct orders of the results even when it is applied to turbulent flows and is used here to evaluate the scaling of the surface stress and critical film thickness for instability.

The surface stress is evaluated by Benjamin's quasi-laminar method (Craik, 1966):

$$\Sigma_i = \rho V_s^2 (\beta I / c_f) \alpha^3 (\alpha \text{Re})^{-4/3}, \quad (19)$$

$$\Pi_r = \rho V_s^2 \frac{\alpha I}{Rc_f}, \quad (20)$$

where $\alpha = kh$. The expressions for I and β are

$$I = \int_0 (u(y)/U_0) e^{-\alpha y} d(\alpha y), \quad (21)$$

$$\beta = 1.188 \left(\frac{V_g}{v} \right)^{2/3} \left(\frac{\rho_g}{\rho} \right), \quad (22)$$

where $u(y)$ is gas velocity profiles given by Eq. (11).

The critical thickness below which instabilities occur is found approximately 5.6×10^{-4} m if the parameters in Table 1 are used. The wave number k is evaluated as $k = 2\pi f / V$, where f is the striation frequency. The molten layer thickness is about one order of magnitude below the calculated critical thickness. The molten front is thus unstable and waves will generate at the cutting front.

Table 1: Physical Quantities and Parameters Used in the Simulation

$U_0 = 340$ m/s	$\mu_g = 4.5 \times 10^{-5}$ kg/(ms)
$b = 0.4 \times 10^{-3}$ m	$\rho = 7.8 \times 10^3$ kg/m ³
$f = 230$ s ⁻¹	$\rho_g = 0.23$ kg/m ³
$\gamma = 1.0$ kg/s ²	$v = 0.64 \times 10^{-6}$ m ² /s
$\mu = 5 \times 10^{-3}$ kg/(ms)	$v_g = 2.25 \times 10^{-4}$ m ² /s

3.2 Prediction of striation frequency

In the aforementioned physical model, the striation frequency is equivalent to the oscillation frequency of melt ejection and oxidation. Under high speed cutting conditions, the frequency should be equivalent to the slow wave frequency. The wave number of the slow wave is approximately taken as the critical wave number at which the mean shear stress τ attains the minimum value. Undamped disturbances for the liquid film of thickness h are sustained at such a minimum value. Substituted by the proper stress evaluation, Eq. (18) becomes

$$\frac{I}{c_f} \left[\frac{k\tau}{\rho} + \frac{3\beta v^{2/3}}{2h} \left(\frac{k\tau}{\rho} \right)^{2/3} \right] = \frac{\gamma k^2}{\rho}. \quad (23)$$

Taking derivative $\partial\tau/\partial k$ of the above equation, one obtains the positive critical wave number:

$$k = \frac{I\tau}{4c_f\gamma}. \quad (24)$$

The mean stress is evaluated according to

$$\tau = \mu \frac{V_s}{h}. \quad (25)$$

The experimental measurement shows that wave speed is about 0.8 of the interfacial velocity (Craik, 1966). The wave frequency is then

$$f = 0.8V_s k / 2\pi. \quad (26)$$

The interfacial velocity V_s is obtained from Eq. (13). To obtain the values of film thickness h as a function of cutting speed and gas velocity, the approach given by Vicanek *et al.* (1986) is used in calculation. In their method, they treated the molten front as a plane and solved the momentum equations based on boundary theory, taking the physical properties at the wall temperature instead of solving the energy equation.

4. Results and Discussions

4.1 Striation frequency and depth

Experiments were carried out for oxygen assisted cutting of 1.6 mm thick steel AISI 1018 with a CO₂ laser. The laser is operated in TEM₀₀ mode with laser power kept at 500 W. The gas pressure was held at 2.1 bar (30 psi, measured on gauge). The cutting speed was varied from 15 mm/s to 50 mm/s. Striation wavelength and depth were obtained by using a Talysurf profilometer taken 0.5 mm from the top of the cut edge.

The predicted striation wavelength and the experimental results are compared in Fig. 5 and they are in reasonable agreement. The increase in cutting speed causes the liquid film thickness and thus the interfacial velocity to increase. As a result, the striation frequency increases, but not as much as the increase of the cutting speed. The net result, therefore, is that the striation wavelength increases with the cutting speed.

Striation depth is evaluated using Eq. (15). This assumes that the parabolic growth of the oxide layer is directly related to the striation depth. The experimental measurement of striation depth is obtained by calculating the peak to peak value of each waveform of striation profile taken from the Talysurf, and then taking the arithmetic mean of these values. Fig. 6 shows the predicted maximum striation depth against the experimental measurements. The coefficient in Eq. (15) is calibrated to be a constant of 4×10^{-8} . The increase of the striation frequency with the cutting speed gives a shorter interaction period for the oxidation and the melting process, thus reduces the striation depth.

4.2 Steady state results of simulation

In our preliminary calculation, the variation of temperature and oxygen concentration at the gas-liquid interface was found insignificant along the direction of workpiece depth for thin workpiece (2mm for our calculation). For simplification, the top and bottom boundaries are assumed to be under insulation conditions. Thus, the 2D calculation is equivalent to that of 1D. All the results shown in this paper are of one dimension in the direction perpendicular to the gas-liquid interface. The incoming laser heat is assumed to be focused down to a point and directly applied in the direction mentioned above. A laser heat flux of 1.2×10^8 W/m² is used in computation. Oxygen purity varies from 1.0 to 0.9, pressure from 2 to 3 bars, cutting speed from

20 to 55 mm/s in the computation. The workpiece thickness is assumed to be 2.0 mm and the type of impurity investigated includes nitrogen and helium.

Fig. 7 shows the temperature profile with different oxygen purity. As mentioned early, reaction is assumed to take place at the gas-liquid interface for the steady state calculation and the temperature is therefore highest at the interface. The temperature quickly drops to the ambient level at the center of the gas stream because of the large diffusion effect due to the temperature-dependent heat conductivity.

Fig. 8 depicts the profile of oxygen concentration with different oxygen purity. A small decrease of purity brings about a large drop of oxygen concentration at the interface, thus reducing the reaction energy because the impurity quickly increases the resistance to further oxygen diffusion when oxygen is being consumed as mentioned previously.

Fig. 9 shows the effects of oxygen purity on cutting speed. As seen, the cutting speed is highly sensitive of small levels of contamination in the oxygen jet, which is consistent with the experimental results given by Powell, *et al.* (1992). This sensitivity comes from the quickly accumulated gas diffusion film when oxygen impurity increases, which is mentioned early. In real cutting cases, the small amount of inert gas may exist in original oxygen supply or may come from the entrainment of the environmental air due to turbulence of the gas jet. The effects of various gaseous impurities are also shown in Fig. 9. The impurity *He* has less effect than that of *N₂* because its smaller molecular weight and diffusion volume result in a larger diffusion coefficient (refer to Eq. (16)), and consequently more oxygen flux for reaction, which is confirmed by experimental observation (Gabzdyl and Morgan, 1992).

The calculated reaction heat, absorbed laser heat and conduction loss into solid versus cutting speed are shown in Fig. 10. At lower speeds, the reaction energy contributes nearly half of the

total energy input and the heat conduction loss takes about half of the total heat loss, which agrees with the results of other researchers (Vicanek and Simon, 1987, Schulz, *et al.*, 1993). At higher speeds, the laser beam has better coupling at the molten front therefore its relative higher contribution towards total energy input increases.

4.2 Dynamic results of simulation

The removal of the oxide layer under hydrodynamic instability is also a complicated process and its detailed, quantitative prediction is beyond the scope of this calculation. We assume the process happens in a short time so that once the oxide layer grows to a certain point, the oxide layer is suddenly removed. After it is removed, the oxide layer starts to grow again. The period of this growth-removal cycle is obtained from the calculated wave period. Fig. 11 shows typical cycles of front temperature fluctuation. The coefficient of the parabolic growth is not readily available and therefore it is calibrated so that the temperature fluctuation is around a level obtained from experiments (Arata, *et al.*, 1979). When the oxide layer starts to grow, oxidation slows down because of the high resistance of the oxide layer to the oxygen diffusion, and the temperature starts to drop. Once the oxide layer is removed, the temperature quickly picks up due to a sudden increase of oxygen flux and reaction energy.

The temperature fluctuation is also inherently linked to molten layer fluctuation since the phase change produces a heat sink in the process. As shown in Fig. 12, the calculated molten layer fluctuation caused by the temperature fluctuation shows a similar pattern as the experimental observation of the cut front mobility captured by the high speed photography. Since in our calculation, the thickness of the molten layer is obtained by summation of the grids where phase change takes place, the accuracy is limited by the grid size and the calculated

thickness is somewhat stepwise. Given the limited resolution of high-speed photography, the discrepancy between the experimental and numerical results is considered acceptable.

5. Concluding Remarks

The model developed in this paper describes the process of the oxygen-assisted cutting of mild steel and the numerical simulation quantitatively predicts the effects of oxidation. The numerical results show the transport phenomenon in the gas stream can not be neglected and thus give an explanation why a small amount of oxygen impurity will greatly reduce cutting speed. The formation of striation is related with the unstable behavior of the oxide layer caused by hydrodynamic instability. The striation frequency is predicted accordingly. The oxidation energy is very sensitive of the oxide layer that has a large resistance to oxygen diffusivity. With the oxide layer oscillation based on the instability theory, the striation phenomenon is simulated via transient temperature fluctuation and the molten layer fluctuation.

Nomenclature

B: constant in Eq. (14)
c: molar density
 c_p : heat capacity
 c_f : friction factor
D: diffusion coefficient
 E_a : activation energy
f: striation or wave frequency
h: thickness of molten layer or sensible enthalpy
H: kerf width
I: defined in Eq. (21)
K: thermal conductivity
 K_e : equilibrium constant
k: wave number
 k_r : kinetic rate coefficient
M: molecular weight
N: mass flux

P: gas pressure
 P_l: laser power density
 q_r: reaction heat flux
 q_l: laser heat flux
 r: distance from laser beam center
 r_l: beam radius
 R: universal gas constant
 Re: Reynolds number of liquid, $Re = V_s h / \nu$
 s: thickness of the oxide layer
 T: temperature
 t: time
 U₀: bulk gas velocity
 u: cutting speed in x direction
 v*: friction velocity
 V: diffusion volume
 v: velocity in y direction
 V_s: surface velocity
 x: distance perpendicular to melt flow
 X_{o2}: oxygen concentration
 y: distance along melt flow
 α: $\alpha = kh$
 β: defined in Eq. (22)
 ρ: density
 ν: kinematic viscosity
 δ: thickness of gas diffusion film
 μ: viscosity of melt
 τ: mean stress
 γ: surface tension
 Π_r: normal stress parameter
 Σ_i: tangential stress parameter
 ΔG_{rx}: standard Gibbs free energy
 ΔH: latent heat content
 ΔH_R: reaction energy

Subscripts:

l: liquid
 g: gas
 m: melt
 o₂: oxygen; n₂: nitrogen
 e: equilibrium
 0: interface between gas and melt
 i: reaction front
 δ: gas diffusion film
 h: molten front

References

- Arata, Y., *et al.*, "Dynamic behavior in laser gas cutting of mild steel", *Trans. JWRI*, Vol. 8(2), 1979, pp. 15-26.
- Benjamin, T. B., "Shearing flow over a wavy boundary", *J. Fluid Mech.*, Vol. 6, 1959, pp. 161-205.
- Birks, N., and Meier, G. H., *Introduction to High Temperature Oxidation of Metals*, Edward Arnold, London, 1983.
- Cai, L., and Sheng, P., "Analysis of laser evaporative and fusion cutting", *J. of Manufacturing Science and Engineering*, Vol. 118, 1996, pp. 225-234.
- Chen, K., Yao, Y. L., "Striation formation and melt removal in laser cutting process", *J. of Manufacturing Processes*, Vol. 1, No. 1, 1999, pp. 43-53.
- Chen, K., Yao, Y. L., and Modi, V., "Numerical simulation of oxidation effects in laser cutting process", *Int. J. Advanced Manufacturing Technology*, in press.
- Craik, A. D. D., "Wind-generated waves in thin liquid films", *J. Fluid Mech.*, Vol. 26, 1996, pp. 269-292.
- Di Pietro, P., Yao, Y. L., "A numerical investigation into cutting front mobility in CO₂ laser cutting", *Int. J. Mach. Tools Manufact.*, 35(5), 1995, pp. 673-688.
- Di Pietro, P., Yao, Y. L., and Chen, K., "An experimental study of on-line estimation of striations in laser cutting process", *Technical Papers of NAMRI*, 1997, pp. 105-110.
- Espinal, D., and Kar, A., "Representation of chemical reaction in laser cutting", *ICALEO'98*, Vol. 85, Part 1., pp. 68-77.

- Fukaya, K. and Norio K., "Analysis of CO₂ laser beam suitable for thick metal cutting", *ICALEO '90*, pp61-70.
- Gabzdyl, J. T. and Morgan, D. A., "Assist gas for laser cutting of steels", *ICALEO'92*, PP. 443-448.
- Ivarson, A., *et al.*, "The oxidation dynamics of laser cutting of mild steel and the generation of striations on the cut edge", *J. of Materials Processing Technology*, Vol. 40, 1994, pp. 359-374.
- Modest, M. F., and Abakians, H., "Evaporative cutting of a semi-infinite body with a moving CW laser", *ASME J. of Heat Transfer*, Vol.108, 1986, pp. 602-607.
- Molian, P. A., and Baldwin, M., "Combustion-assisted laser cutting of a difficult-to-machine superalloy," *J. of Laser Applications*, Vol. 4, No. 1, 1992, pp. 9-15.
- Patankar, S. V., *Numerical Heat Transfer and Fluid Flow*, Taylor & Francis Publishers, 1980.
- Powell, J., *et al.*, "The role of oxygen purity in laser cutting of mild steel", *ICALEO '92*, pp. 433-442
- Schulz, W., *et al.*, "Heat conduction losses in laser cutting of metals", *J. Phys. D: Applied Phys.* Vol. 26., 1993, pp. 1357-1363.
- Themelis, N. J., *Transport and Chemical Rate Phenomena*, Gordon and Breach Publishers, 1995.
- Vicanek, M., and Simon, G., "Momentum and heat transfer of an inert gas jet to the melt in laser cutting", *J. Phys. D: Appl. Phys.*, Vol. 20, 1987, pp. 1191-1196.
- Vicanek, M., *et al.*, "Hydrodynamic instability of melt flow in laser cutting", *J. Phys. D: Appl. Phys.*, Vol. 20, 1986, pp. 140-145.

Yilbas, B. S., and Sahin, A. Z., "Oxygen-assisted laser cutting mechanism - a laminar boundary layer approach including the combustion process, *Optics and Laser Technology*, Vol. 27, No. 3, 1995, pp. 175-184.

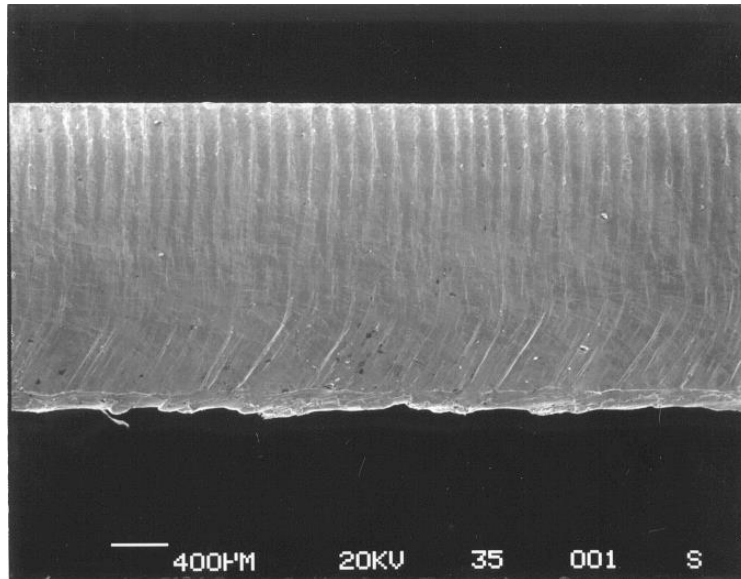


Fig. 1: Typical cut edge showing striation pattern in thin sections

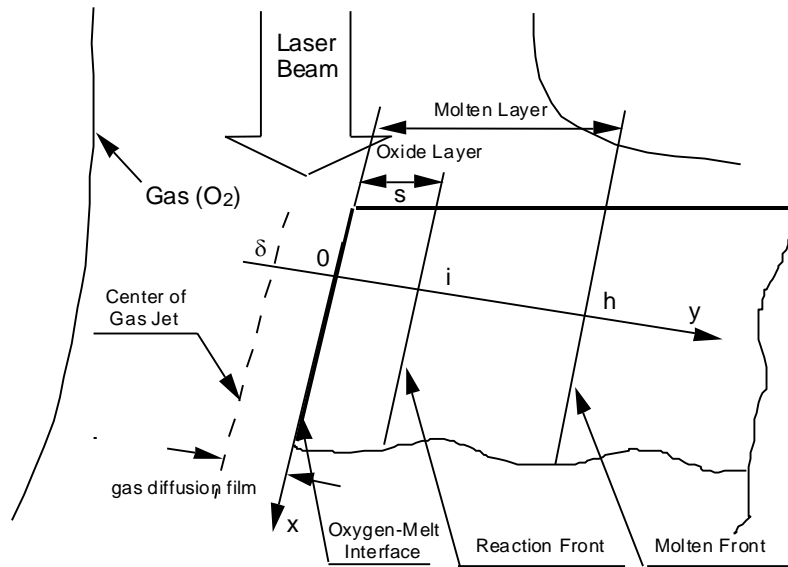


Fig. 2: Oxidation model

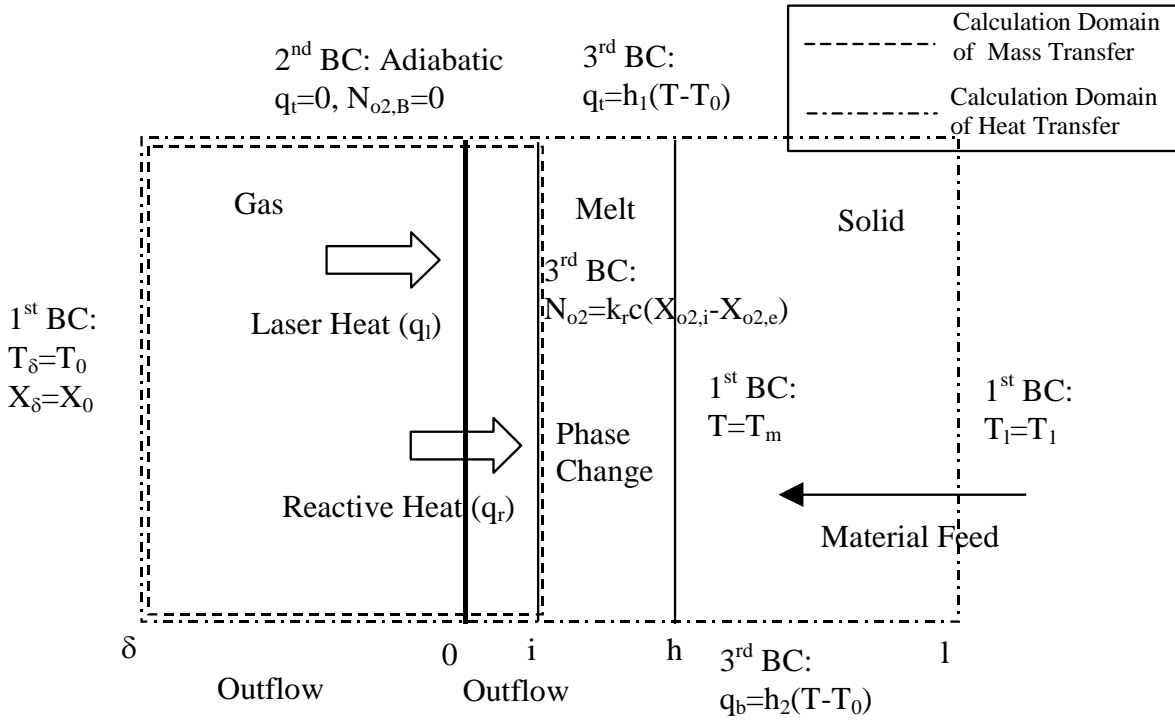


Fig. 3: Calculation domain and boundary conditions

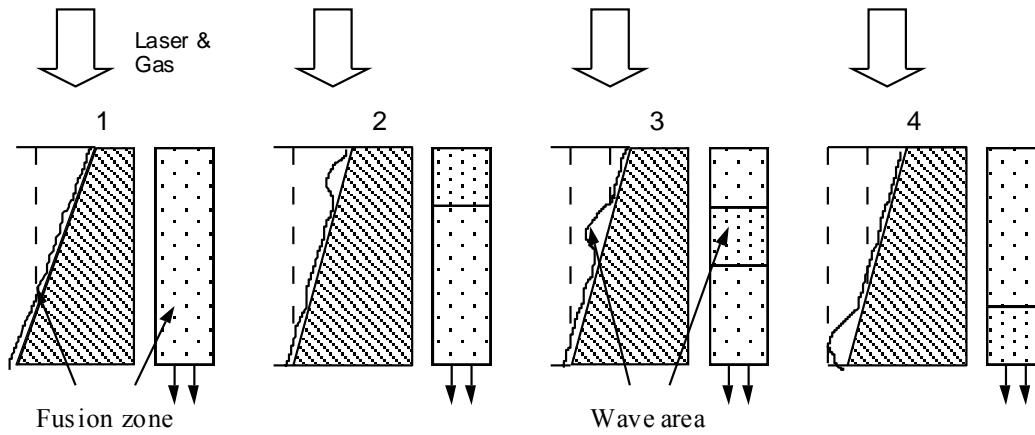


Fig. 4: Schematic of the molten front change at high cutting speeds

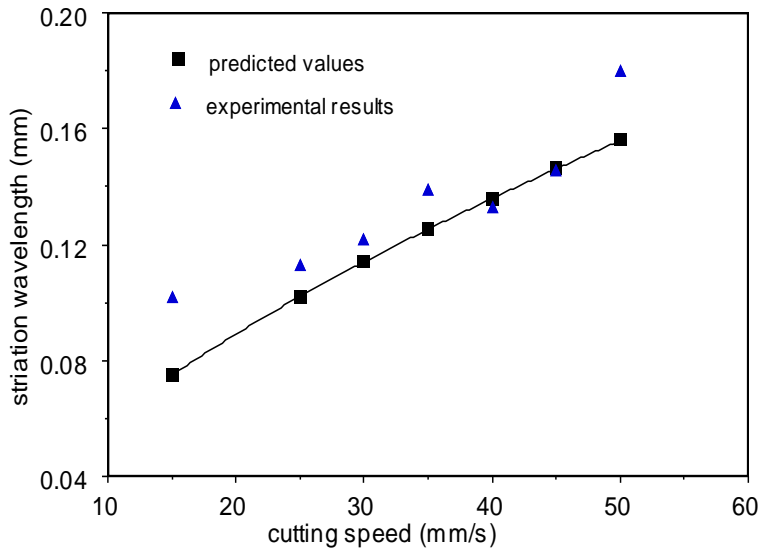


Fig. 5: Striation wavelength versus cutting speed

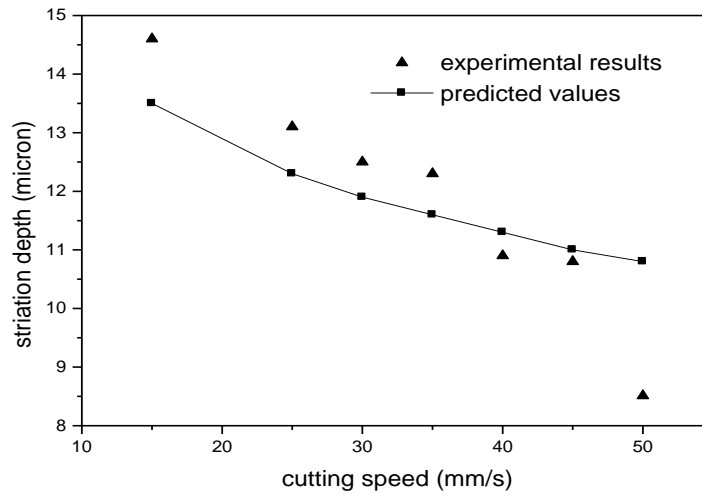


Fig. 6: Maximum striation depth versus cutting speed

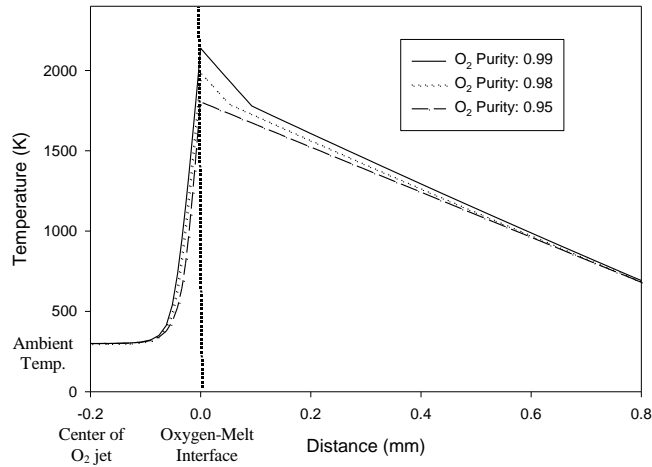


Fig. 7: The temperature profile with different oxygen purity (Laser Heat Flux=1.2e+08 W/m², Oxygen Pressure=2.5 Bar, Cutting Speed=45 mm/s)

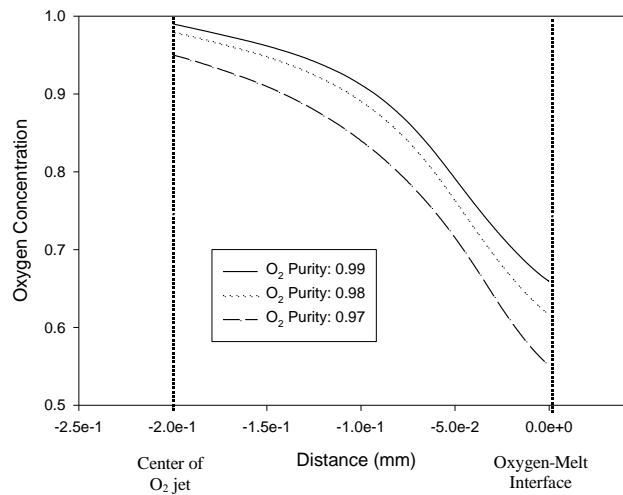


Fig. 8: Oxygen concentration profile with different oxygen purity (Laser Heat Flux=1.2e+08 W/m², Oxygen Pressure=2.5 Bar, Cutting Speed=45 mm/s)

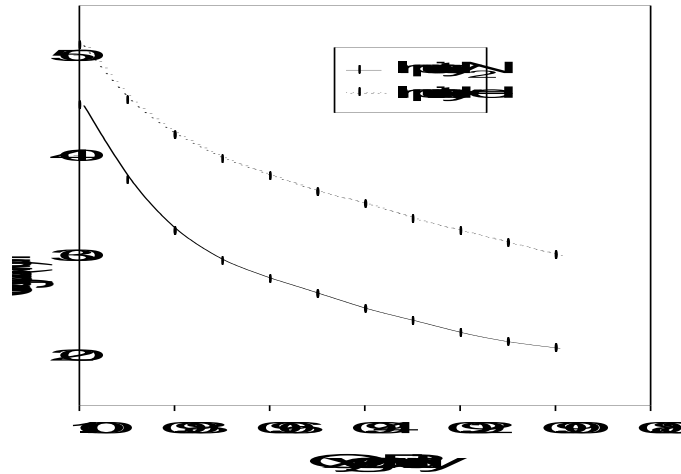


Fig. 9: The effects of oxygen purity and impurity type on cutting speeds (Laser Heat Flux=1.2e+08 W/m², Pressure=2.5 Bar)

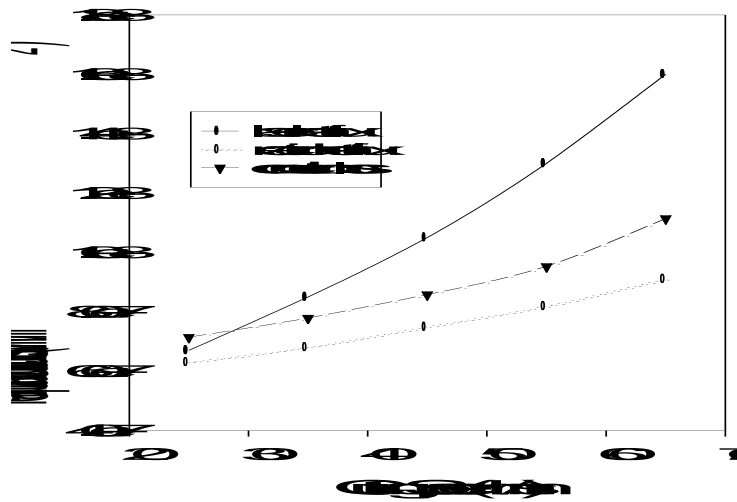


Fig. 10: Heat input and loss versus cutting speed (Oxygen Purity = 0.995, Pressure = 2.5 Bar)

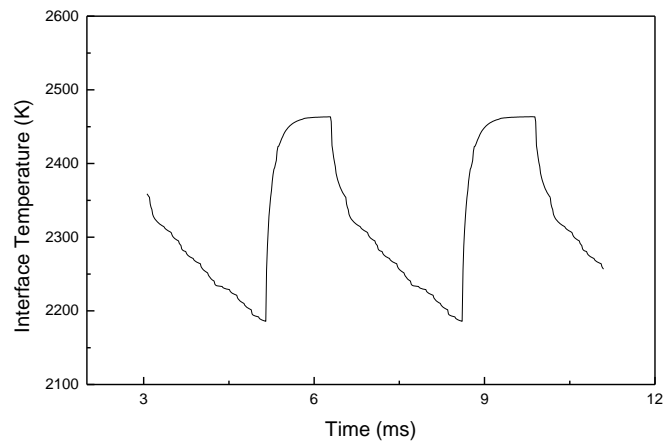


Fig. 11: The temperature fluctuation at the oxygen-melt interface (Laser Heat Flux= 1.2×10^8 W/m², Pressure=2.5 bar, Cutting Speed =35mm/s)

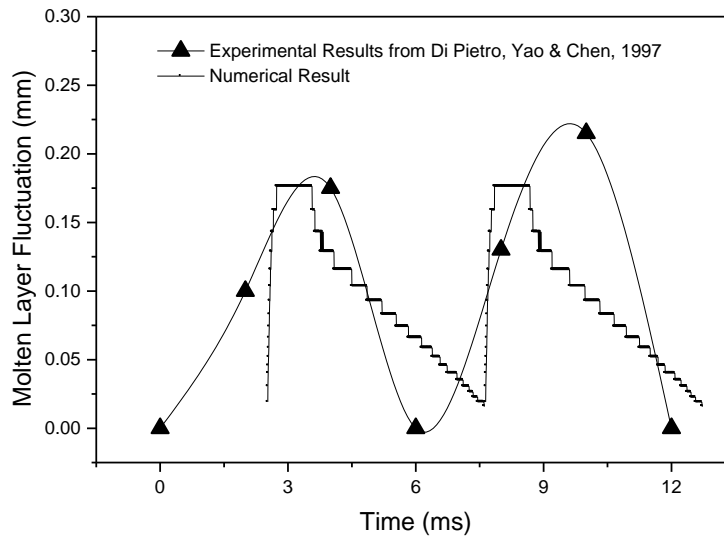


Fig. 12: Molten layer fluctuation
(Laser Heat Flux = 1.2×10^8 W/m², Pressure = 2.5 bar, Cutting Speed = 25 mm/s)